States of functional connectivity flow and their multiplex dynamics in human epilepsy and postictal aphasia

Nicola Pedreschi[1,2,3,⋆], Agnès Trebuchon[2,4], Alain Barrat[1], and Demian Battaglia[2,5]

1 Aix-Marseille Univ, Université de Toulon, CNRS, CPT, Turing Center for Living Systems, Marseille, France

2 Aix-Marseille Université, Inserm, INS, Institut de Neurosciences des Systémes, Marseille, France

3 Mathematical Institute, University of Oxford, Oxford, UK

4 Assistance Publique Hôpitaux de Marseille (APHM), Service d'épileptologie, Marseille, France

5 University of Strasbourg Institute for Advanced Studies (USIAS), Strasbourg, France

⋆ nicola.pedreschi@maths.ox.ac.uk

Abstract

The mechanisms that cause aphasia as a transient post-seizure symptom in epileptic patients are yet unknown. We analyse intracranial EEG (sEEG) recordings of patients suffering from pharmaco-resistant epilepsy with postictal aphasia. We study the Functional Connectivity (FC) between different cortical sites in a time- and frequency-resolved manner, representing each recording as a time-varying, multilayer network (dynamic multiplex). We studied in particular: the rate of overall reconfiguration of links from one frame to the next, or dynamic Functional Connectivity (dFC) speed; and the stability of network modules through time, by means of a dynamic modular Allegiance (dA) analysis. The combination of these two approaches allows identifying states of "Functional Connectivity flow" (beyond connectivity states), defined as epochs in which network reconfiguration occurs with comparable speed and degree of spatio-temporal coordination. Our unsupervised analyses reveal then that high-frequency dFC is slowed down in a long postictal phase lasting well beyond the ictal episodes themselves. Furthermore, a pathological state of slow and poorly structured network flow consistently co-occurs with episodes of aphasia symptoms annotated by the clinicians. In conclusion, our multiplex network dynamics description cast light on functional mechanisms of postictal cognitive dysfunction at the level of individual patients.

1 Introduction

Epilepsy is a neurological disorder in which brain activity becomes abnormally synchronous [5, 6], first in localized regions then spreading to other zones. As an effect of propagating seizures, unusual behavior and feelings and sometimes even loss of awareness can arise, with the order and nature of symptom appearance informing the neurologist about the possible pattern of propagation of the seizure. It is evident that epilepsy is a network pathology, both because the interested regions are distributed and interacting and because the mechanisms themselves of the pathology are associated to disrupted local and global coupling between neuronal populations [4, 14]. A fact whose impact on the quality of life is often underestimated is that epileptic patients may suffer from cognitive deficits even well beyond the seizures themselves, as if network function alterations were not limited to just the hypersynchronization events associated to the seizure, but were present, in more limited or different form, also during "baseline" conditions [26]. While seizure-related changes may be more prominent, these changes in epochs preceding and following seizures may be transient, subtler and difficult to detect, thus requiring the development of suitable network analysis tools.

Here we analyze intracranial EEG (or stereotaxic EEG, sEEG) recordings in individual epileptic patients, hospitalized and implanted with electrodes in order to better localize the epileptic foci, in prevision of a potential surgery (only treatment available due to the pharmaco-resistance of their specific epilepsy). It is important to stress that the considered recordings are actual clinical data and that no patient is identical to another. Therefore, analyses must necessarily be conducted in a personalized manner for individual patients, without assuming that different cases can be grouped. Despite differences between patients (and even, sometimes, between different seizures for a given patient), our analyses are able to identify some general traits of the network dynamics associated to entering and leaving an epileptic seizure phase and only very gradually and slowly recovering a baseline-like condition. Furthermore they have the sensitivity to characterize specificities at the single patient level.

Specifically, we adopt a time-resolved multiplex network approach, in which different network layers correspond to networks of inter-channel coherence in different frequency bands. Since epilepsy is linked to hypersynchronization, it is natural to adopt a measure of Functional Connectivity tracking oscillatory synchronization, such as wavelet coherence [25]. Synchrony alterations, however, are observed over multiple different coordinated frequency bands (which requires a multiplex network description), including high-frequency bands where power is overall lower, and are transiently manifesting (which requires a temporal network description). Our methods of analysis thus describe

both temporal and multiplex aspects of the measured dynamic Functional Connectivity revealed by recorded signals. We identify, within each network layer, and via an unsupervised approach, a variety of distinct functional connectivity states, which not only happen to relate to a rough staging of the seizure event (pre, during and post seizure), but, furthermore, predict shorter and transient epochs of time during the post-crisis recovery in which language disturbances such as aphasia are reported by the clinician assisting the patients. Beyond single-layer analyses, we show that epilepsy affects the coupling between layers, loosening it in some cases but strengthening it in others. This is an interesting observation in relation to the emergence of language disturbances [17], as language parsing requires the tight coupling between neural dynamics events paced by different frequencies (associated to different language time-scales such as the ones separating phonemes, syllables, words, sentences [20, 30].

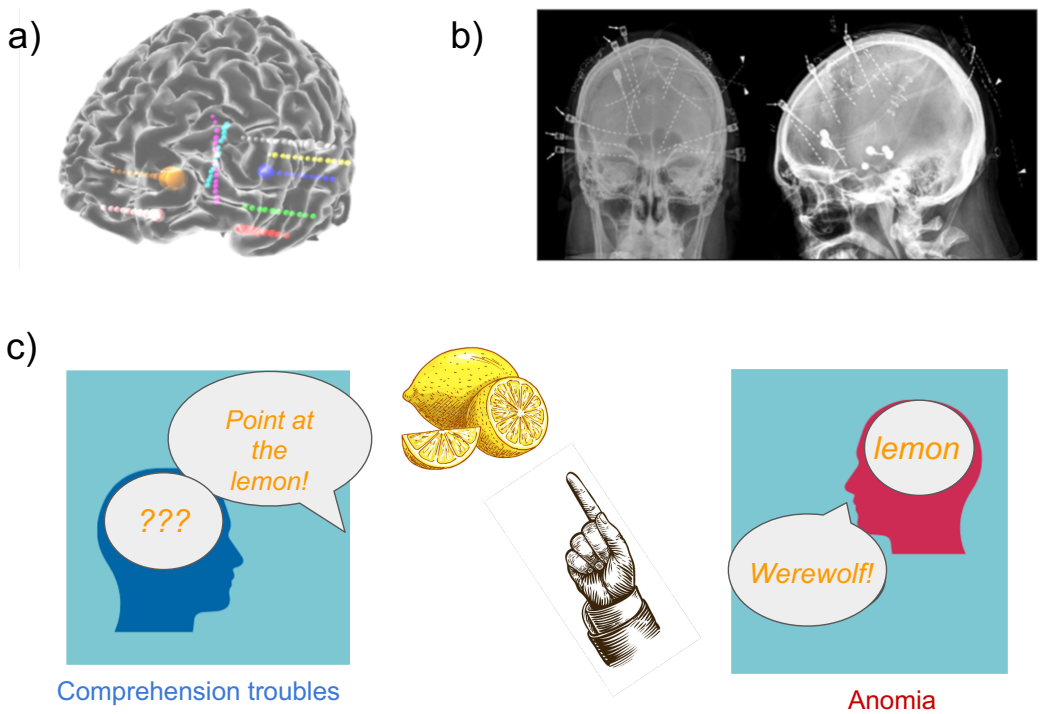

Figure 1. a)-b) Representative 3D reconstruction and X-ray imaging of intracranial stereotactic EEG (sEEG) electrodes implanted in a patient suffering of pharmaco-resistant epilepsy for the sake of pre-surgical investigations and determination of the epileptogenic zone. Intracranial recordings are performed over long durations reaching several hours, including one or more seizure events, surrounded by pre-ictal and post-ictal periods. The positioning of multiple electrodes allows recording simultaneously activity from a variety of temporal, parietal and frontal brain regions (See Table S1). **c)** During the recovery phase following a seizure, transient impairments of the language function (aphasia) are reported by the clinicians. The cartoons represent examples of impairments that can be detected through the testing of language comprehension (left) and language production (right).

An important novel aspect of our approach is that we characterize dynamic network states not only in terms of their state-specific connectivity patterns (such as e.g. a distinct modular partition for each state) but also in terms of their "style" of reconfiguration of connectivity. Indeed, functional connectivity is never frozen, but keeps constantly reorganizing even within each of the states. Fluctuations around the state-specific multiplex connectivity patterns can be more or less structured, and occur through larger or smaller network variation events. We characterize the properties of within-state network dynamics: i) inspecting whether fast connectivity fluctuations maintain or disrupt the *module allegiance* pattern of different network nodes (i.e. whether different regions, in their flow across dynamically changing network structures, tend to remain within matching or distinct modules); and ii) quantifying the instantaneous rate of variation of functional networks, via a suitably defined measure of connectivity reconfiguration *speed*. So, dynamic connectivity states may differ between them for genuinely dynamic traits, besides time-averaged network topology: dynamics could be fast in certain states and slower in others, or be random-like in some states and preserving the association of certain region pairs despite module reconfiguration in others. Such capacity to directly describe dynamics (and differences among alternative dynamics) crucially allows us to identify baseline as a condition in which networks fluctuate swiftly and in a spatiotemporally ordered manner. Pathological states are on the contrary associated with a loss of this flexibility and organization, even if network fluctuations are never suppressed.

2 Results

2.1 From intracranial SEEG recordings to a dynamic multiplex network

As previously mentioned, we are interested in studying the time-varying functional connectivity of networks in different frequencies of interaction. Indeed, different frequency bands are thought to be involved in the processing of distinct language aspects [20, 30]. For this reason, we compute the wavelet coherence [25] in five different frequency bands between each pair of recorded signals. To do so, we decompose signals in the time-frequency domain along the Morlet wavelet family. The wavelet coherence $W.C.(t, f)$ (see Methods for proper definition) has values between 0 and 1. We compute the wavelet coherence $W.C(t, f)$ for each pair of signals in 5 frequency bands peaked around 1Hz, 5Hz, 10Hz, 20Hz and 40Hz. The coherence values computed for each of the 5 reference frequencies represent, for each pair of signals, 5 time series of temporal edges between the same nodes i and j representing the sources of the signals. We therefore represent these data as a time-varying multi-layer

weighted network, where the weight of a temporal edge $(i, j, t)^l$ at time t, in layer l corresponds to the coherence in frequency band l of nodes i and j at time t. Since the nodes in all layers are the same, we refer to this object as a *temporal multiplex network*. Only significant links are included in the multiplex networks, where a significance threshold is determined in terms of coherence estimated with randomized signals. After signal down-sampling, we maintain a very precise temporal resolution, since, for the faster frequencies, we estimate a different, independent time-resolved network frame every ∼100ms (see *Materials and Methods*). A schematic representation of the extraction of the temporal multiplex from the raw data can be found in Figure 2.

We first present a complete analysis for a representative seizure recording for a specific patient. Focusing on one concrete example, allows us present in detail all the steps composing our complex analysis pipeline, while remaining concise and focused. We then postpone the systematic comparison of results across available recordings to a final last section, remarking since now that most of the results obtained for the chosen representative seizure will be qualitatively confirmed in other recordings as well.

2.2 Layer-wise global network properties

We start our analysis by computing two global network measures on each layer as general indicators of connectivity fluctuations. Such measures are the instantaneous total network strength, namely the sum of edges' weights at each time point, and the layer's modularity, i.e., a quality function $Q(t) \in [0, 1]$ which reflects the tendency of the network's layer to be organised into different modules (communities; in the literature $Q \geq 0.2$ for significant network partition into different modules/communities [18, 32]). In Figure 3.a, we show for each different frequency layer, the time series of the layer-wise instantaneous total strength $s(t)$ (sum of all instant link weights) of the network (blue hues), and the instantaneous modularity $Q(t)$ (orange hues). In Figure 3.a, for the 1Hz layer, the strength s (darkest blue line in the top plot) is persistently close to $N = 117$ (the size of the network), meaning that, in average, each node is connected to almost the entirety of the rest of the network with high values of coherence. This layer of the network is therefore particularly dense, associated to global slow oscillations of the entire system, which causes the values of $Q(t)$ to be extremely low (darkest red line in the bottom plot). This suggests that the 1Hz layer has no modules to be retrieved at any given time.

When increasing the frequency (lines with progressively lighter colors in Figure 3.a), a richer network dynamics start surfacing, also due to lower connection densities. The values of average

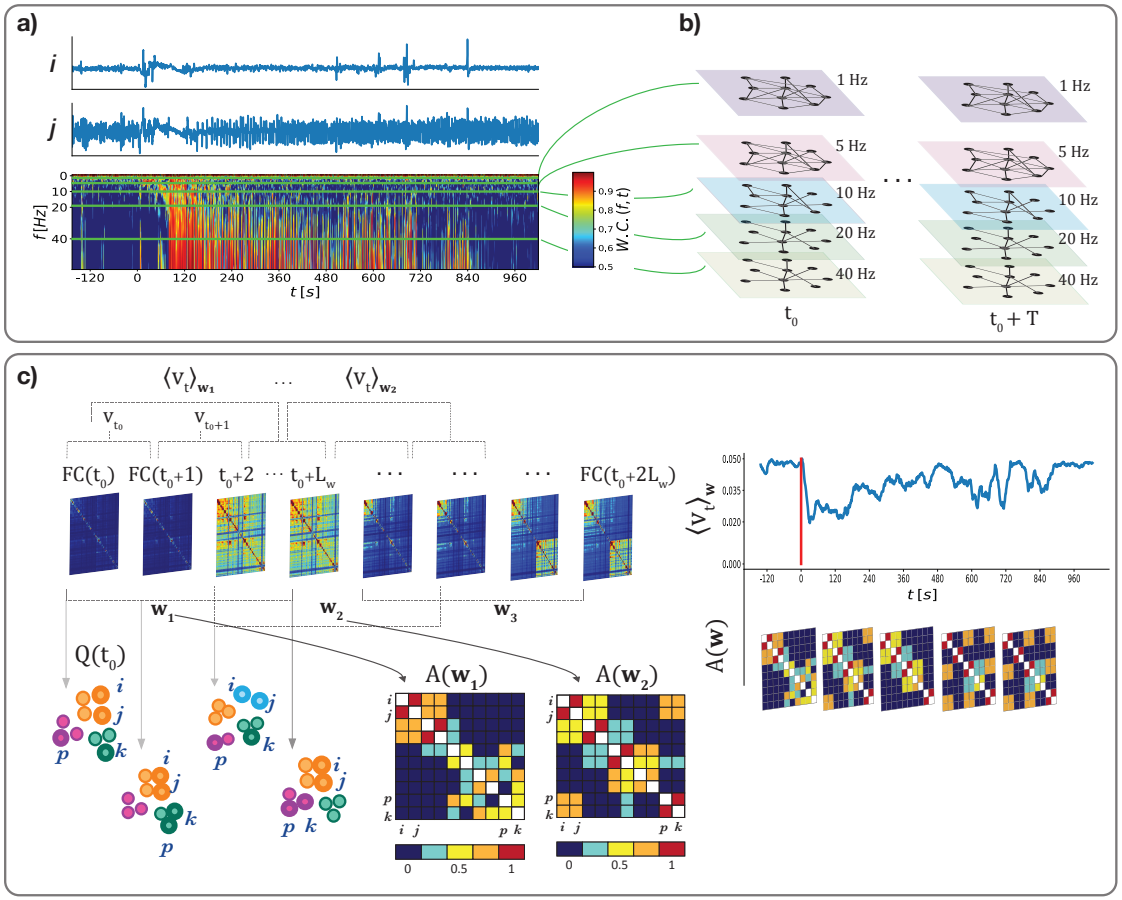

Figure 2. Analysis building blocks: a) Schematic representation of a recording as a dynamic multiplex network; from each pair of signals from different electrode contacts A and B (blue curves on the top left, examples for two representative channels) we compute the *Morlet wavelet coherence* at each time-stamp for a span of frequencies ranging from 1 to 80 Hz; we consider 5 frequencies of interest, $1, 5, 10, 20$ and 40 Hz and follow their dynamics edges in the respective 5 layers (on the right) for each pair of regions. **b** We therefore end up with an instantaneous network for each time-stamp in each of the 5 layers. For each layer (frequency) we generate a series of instantaneous snapshots of the network, i.e., a stream of FC matrices (middle). **c** From each pair of consecutive instantaneous FCs, we compute the rate of change, cosine distance, $\Delta FC(t, t+1)$ from one to the other, which we then average over a larger window w, including L_w time-frames. This procedure yields a window-resolved estimation of average network reconfiguration *speed* $\langle V_t \rangle_w$ (schematic representation on the top). At each time point, we partition the network into its modules, and computing the associated modularity $Q(t)$ (bottom-left cartoon). Within each window w, we compute the corresponding allegiance matrix $A(w)$, whose entries report the probability that each considered pair of network nodes (i and k in the cartoon). For each layer we finally end up with a time series of network reconfiguration speed $\langle \Delta FC(t, t+1) \rangle_w$ matched to a stream of allegiance matrices $A(w)$ (right).

strength in the 5Hz layer are lower than those of the 1Hz layer. Eventually, the layer undergoes a sharp increase in average strength at seizure onset, which then rapidly decreases to baseline values, even before any of the reported clinical marker. The modularity values of the same layer are below $Q \sim 0.2$ for the entirety of the recording, yet a substantial drop of Q is observed in correspondence to

seizure onset, thus coinciding with the increase in strength. The two time series of total strengths and modularity are anti-correlated for the other layers as well, as the emergence of additional transient links contribute to reduce the segregation between modules: for the 10Hz layer, the trend of the two curves is remarkably similar to the one of the 5Hz layer, with lower values of $s(t)$ and higher values of $Q(t)$; however, this layer resumes baseline strength and modularity values slightly later than the 5Hz one.

The tendency to have increasingly longer times for return to baseline values with increasing frequency, is confirmed by the other higher frequency layers as well. For the 20Hz layer (Figure 3.a, lightest colors) the return to baseline values is markedly slower, particularly for its modularity and even happens after the last clinical marker at which symptom follow-up by the clinicians is stopped considering that the post-ictal phase has been overcome. Dramatically slower is then the return to baseline values for the 40Hz layer, in Figure 3.b. For this layer, the perturbation induced by the seizure lasts the longest, as, in the considered example, baseline levels of network activity are resumed only in the last three minutes, well beyond the reported end of the seizure. We show analogous analyses of strength and modularity for other recordings in Supplementary Figure **S2**. Note as well that qualitatively similar trends are observed when constructing networks in terms of time-series from a bipolar montage (see Supplementary Figure **S3**) for a direct comparison). We chose here however to focus on simpler unipolar montages, because the larger number of nodes they provide, despite the larger noisiness and uncorrected volume conduction, allows better emphasizing network structure in the high frequency layers (see *Discussion*).

2.3 Comparing network flows, beyond networks: dynamic Modular Allegiance analysis

As mentioned in the previous section, we carry on our layer-wise analysis at two different time-resolutions: a first, faster, corresponding to the separation between individual estimated network frames; and a second, slower, set by a sliding window analysis with windows including $L_w = 200$ time points (thus approximately $L_w =\sim 2.3$ seconds). The adoption of such double resolution allows us to study not only the network organization of individual frames (as in Figure 3) but also the time-dependency of the flow of frame-to-frame network reorganization itself, since a window includes multiple frames and hence a time-localized movie snippet of how Functional Connectivity is changing in a well identified epoch. Within each of these slower time-resolution windows of analysis, we compute the allegiance between each pair of regions, i.e. how coordinated are the reconfiguration flows

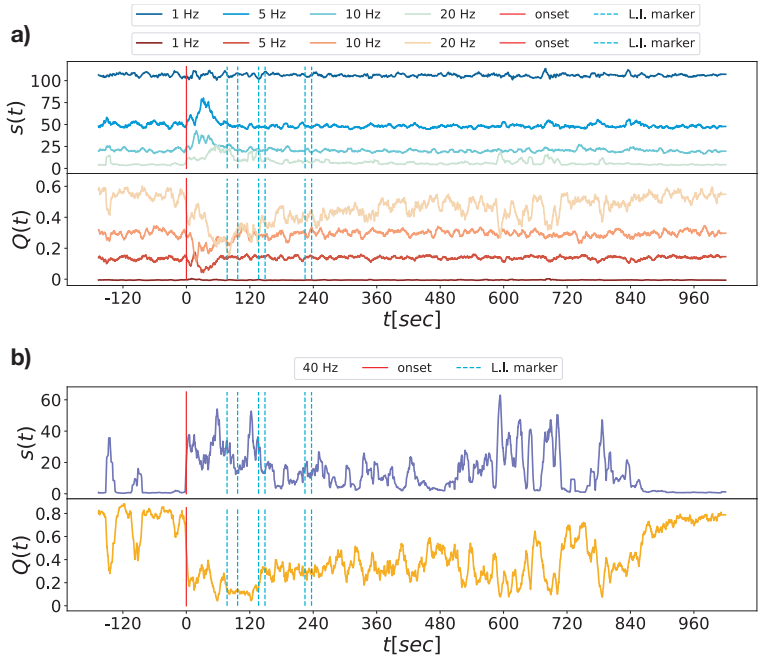

Figure 3. Strength and Modularity time series: a) We show, for a representative recording, time series of instantaneous total strength $s(t)$ (top, blue colors) and modularity $Q(t)$ (bottom, red colors) of four frequency bands (in progressively lighter colors from slower to larger frequencies, namely: the 1Hz, 5Hz, 10 Hz and 20Hz layers. In b), we show with greater detail, $s(t)$ and $Q(t)$ time-series for the highest-frequency layer at 40Hz. The vertical lines in the plots represent the clinical markers: the seizure onset in red, and the language dysfunction markers are represented by the cyan dotted lines. See Supporting Figure S2 for other recordings and Supporting Figure S3 for comparison between uni- and bipolar montages.

of the two regions in the pair, dynamically shifting between different network modules transiently materializing and updating (as we will soon explain in more detail, see *Materials and Methods* for precise definition). The result is a different *allegiance matrix* $A(w)$ for each time-window w , whose matrix element $A_{ij}(w)$ corresponds to the probability of observing regions i and j in the same module (community) over the duration of the time window w (see Figure 2.c). We then smoothly slide the window producing for each layer, as a result, a temporally-ordered series of allegiance matrices, each corresponding to the relative time window. Through this double resolution access we thus get a simultaneous description of network dynamics within each window and of "dynamics of network dynamics" across the different windows.

Allegiance analysis within each window captures the more or less marked tendency of different nodes to *move* in time across different modules in a coordinated or independent manner. At each time-frame within the window, a different network is estimated which could thus have different modular partitions. The fast network reconfiguration dynamics may affect modular structure differently. It may be that because of network reconfiguration, previous-time modules are dissolved and regenerated

near-randomly without specific memory. In that case, the probability for any pair of network nodes to be systematically assigned to a same transient module (independently from which one this module is) would be low and at chance level, resulting in unstructured within-window allegiance matrices with small entries. However, the module reconfiguration could also occur in a more organized manner. Notably, regions may still be floating across modules but do it in coordinated groups, rather than independently one by one, so that entries with larger values can appear in the allegiance matrix. The average value of within-window module allegiance thus tell us whether module reconfiguration is more or less random and the block structure of the allegiance matrix tells us which are the nodes that tend to co-move across modules while module change and morph, as in a form of "liquid-like" flow (to be opposed to the more "gas-like" random reconfiguration snippets within low-allegiance time windows).

The style itself of module reconfiguration could change in time and become more or less "gaseous" vs "liquid". To detect these changes in dynamics style, one need to compare directly the dynamics. This can be done by computing the cosine similarity (see *Materials and Methods* for formal definition) between allegiance matrices computed within different time windows. These cosine similarities can then be compiled into a matrix, describing similarity between allegiance matrices observed at any possible pair of times, which we call the *dynamic Module Allegiance matrix* (dA). This construction is analogous to the so-called *dFC matrix* (Figure 4.a) introduced to compare fMRI-based transient resting-state networks [9, 28] or to the recurrence matrix probing the evolution of sharing network topology in time [13, 37]. However, here we do not compare connectivity but connectivity flows, whose internal spatio-temporal organization is summarized by the time-resolved allegiance matrices. So, fast variations of network connectivity within each window are captured by time-resolved allegiance analysis and slower variations of network dynamics across windows are captured by the dynamic modular allegiance matrix.

The layer-wise dynamic Allegiance matrix, dA^l, shown in Figure 4.a for the 40Hz frequency band, is obtained by computing the cosine similarity between pairs of allegiance matrices computed in two different time windows t and t^*. The matrix element $dA^l(t, t*)$ ranges from 0, when the two allegiance matrices in windows t and t^* are completely different, to 1, when the two are exactly identical. The block-wise structure of a layer's dA suggests the existence of epochs, or states [29], in which the allegiance matrices computed in the corresponding time windows are similar: these are states in which the allegiance dynamics of regions is in a stable and persistent regime, that we refer to as *allegiance states*. We cluster the layer-wise tensor of allegiance matrices A_{ijt}, whose element for

$t = t^*$ corresponds to the allegiance matrix computed in the t^*th window, by means of a spectral clustering, using the dA as pre-computed distance matrix among the different windows along the time dimension.

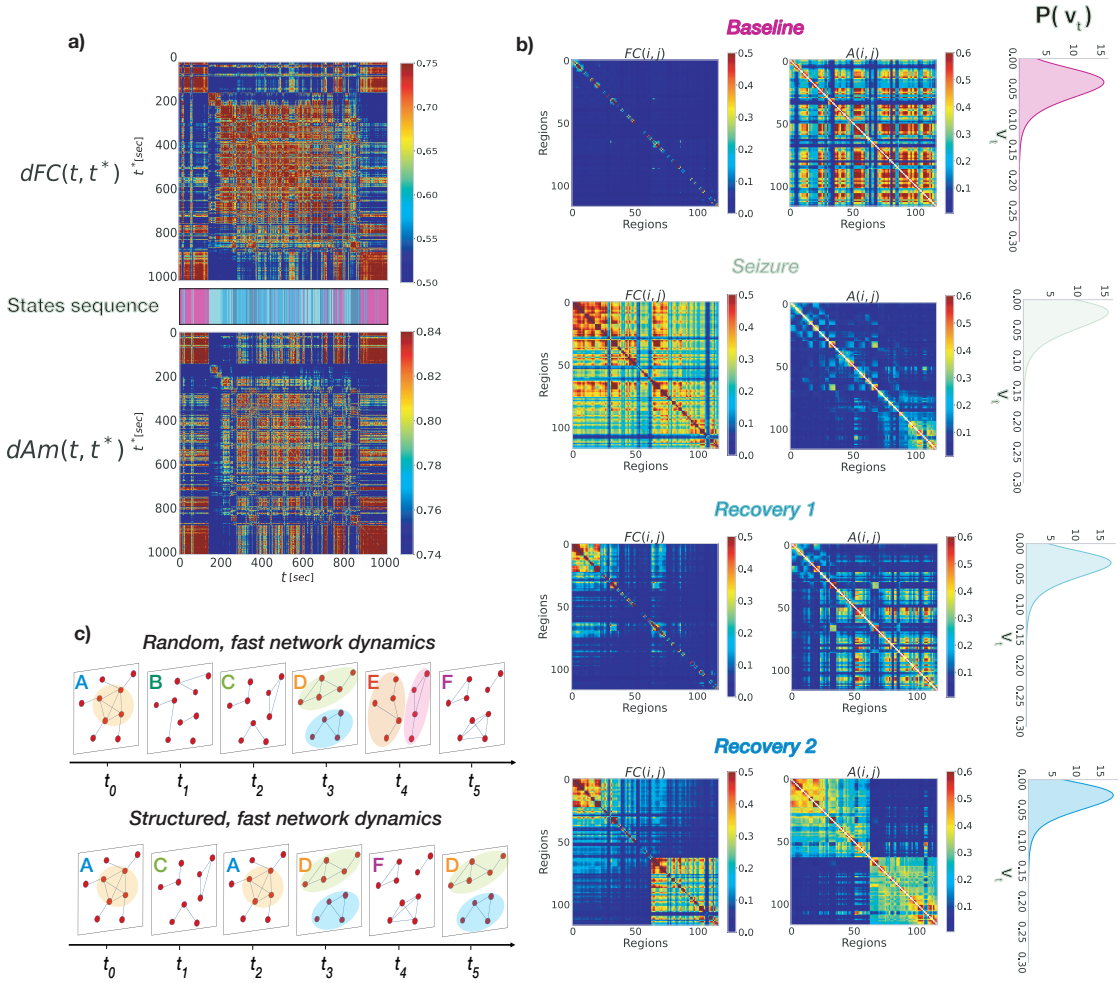

Figure 4. Allegiance dynamics and allegiance states:a) dynamic Functional Connectivity (dFC) matrix (top) and dynamic Allegiance (dA) matrix, bottom, computed for the 40Hz frequency band of the representative recording. **b)** Each row corresponds to one of four retrieved allegiance states, namely, Baseline, Seizure, Recovery 1 and Recovery 2, and the three plots on a row are, from left to right, the corresponding average Functional Connectivity matrix, the corresponding average modular allegiance matrix and the distribution of dFC-speed values measured within the corresponding state. In **c)** is a cartoon comparison of different flows of network dynamics that our pipeline allows us to capture: for instance we can distinguish a fast, random rewiring of the network and re-organization of the communities lying within it, from a more structured dynamics.

2.4 Modular allegiance states

In Figure 4.b we display the four allegiance states (clusters of time-windows in dA) retrieved for the 40Hz band of a representative patient. The colormap in the left matrix in each row of Figure 4.b

Table 1. Brain regions and relative electrodes count for the three patients

Brain area	Patient 1	Patient 2	Patient 3
Frontal Operculum Cortex	3	5	3
Frontal Orbital Cortex	7	5	3
Frontal Pole	6	34	23
Inferior Frontal Gyrus, pars opercularis	2	6	3
Inferior Frontal Gyrus, pars triangularis	1	2	0
Inferior Temporal Gyrus, posterior division	31	5	0
Insular Cortex	7	1	21
Middle Frontal Gyrus	5	5	25
Middle Temporal Gyrus, anterior division	5	17	5
Middle Temporal Gyrus, posterior division	16	16	0
Parahippocampal Gyrus, anterior division	8	5	5
Parahippocampal Gyrus, posterior division	3	2	0
Planum Polare	2	2	8
Superior Temporal Gyrus, anterior division	0	3	9
Temporal Fusiform Cortex, anterior division	5	1	0
Temporal Fusiform Cortex, posterior division	16	6	0
Temporal Pole	12	17	8
unassigned	7	20	36
Cingulate Gyrus, posterior division	4	0	4
Inferior Temporal Gyrus, anterior division	8	0	0
Inferior Temporal Gyrus, temporooccipital part	6	0	2
Lingual Gyrus	4	0	3
Middle Temporal Gyrus, temporooccipital part	6	0	5
Precuneous Cortex	2	0	2
Superior Temporal Gyrus, posterior division	2	0	5
Temporal Occipital Fusiform Cortex	7	0	1
Angular Gyrus	0	0	7
Central Opercular Cortex	0	0	5
Cingulate Gyrus, anterior division	0	0	6
Heschl's Gyrus (includes H1 and H2)	0	0	11
Juxtapositional Lobule Cortex (formerly Supplem...	0	0	3
Lateral Occipital Cortex, superior division	0	0	1
Paracingulate Gyrus	0	0	5
Parietal Operculum Cortex	0	0	3
Planum Temporale	0	0	8
Postcentral Gyrus	0	0	8
Precentral Gyrus	0	0	11
Superior Frontal Gyrus	0	0	4
Superior Parietal Lobule	0	0	1

corresponds to the average Functional Connectivity matrix obtained by, first, computing the FC in the same time-windows defined to compute the allegiance matrices, and then by taking the average only on the windows that were assigned to a specific allegiance state, in the case of the first row of Figure 4.b, the *Baseline* state. The matrix in the plot is characterized by overall low values for non-diagonal elements, whereas we see small clusters (blocks) of electrode contacts that are tightly interconnected lying on the diagonal. This suggests that within the baseline state, there are many subgroups of nodes, of small size and involving neighbour electrode contacts, that are persistently tightly interconnected, hence the high values of modularity displayed before seizure onset and at the

end of the recording in Figure 3.b. Such higher connectivity between neighboring contacts may reveal volume conduction, since we chose to analyze unipolar recordings. The right colormap of the first row in Figure 4.b is the allegiance matrix averaged on all the time-windows labeled as *baseline*. The lattice-like structure of this matrix suggests the existence of several groups of nodes with high values of allegiance. Such groups are not exclusively composed of neighbouring electrode contacts because there also marked out-of-diagonal blocks with high values of allegiance. For this seizure recording, thus, the baseline state is associated to a structured allegiance matrix, indicating that the modular structure is not reconfigured in a random manner during the within-window fast network dynamics of baseline state windows. We therefore question whether this modular structure is changing at all.

Indeed, high allegiance values may just indicate that modular structure is constant throughout the window. To discriminate between the cases of a "crystallized" modular partition, where nodes do not change at all their module membership, and the one of a "liquid" reconfiguration where nodes do change module membership but do it in a non-completely random manner, dA analysis is not enough and one must also evaluate whether network is really changing on the fast time-scale within each window. This is done evaluating the rate of instantaneous change of networks within the windows. For each of the allegiance states, we thus also plot the distribution of the rate of change (cosine distance, i.e., 1−cosine similarity) of the instantaneous FC. At every time-stamp t within the considered window, the instantaneous weighed FC is provided by the computation of the wavelet coherence between each pair of regions at the given time-stamp. Then, we compute the quantity $v(t, t+1) \equiv v_t$ which quantifies the variation of instantaneous FC from one time stamp to the next. We compute this variation for all the contiguous time-points included in the considered window and we average it. In this way one can estimate the time-window average rate of change $\langle v_t \rangle_w$ (windowed average dFC speed) with the same time-resolution of the series of allegiance matrices out of which the dA is computed (Figure 2). Overall, from Figure 4.b (top row) we conclude that the baseline allegiance state is not internally frozen, as windows within this state are associated to a distribution of speeds well above zero. On the contrary, as we will see in a comparative analysis between different recordings at the end of the Results section, the baseline state is even the one with higher speed of internal reconfiguration. This means that links do change in time but do it without leading to a fully random reconfiguration of modules, as the allegiance matrix is structured. For other patients, speed of baseline state is always high, however allegiance can be less structured. So baseline state can oscillate between more "gaseous" or "liquid" styles of network reconfiguration. It is nevertheless always very dynamic.

This contrast between a connectivity matrix with weak entries and an allegiance matrix with strong entries is characteristically reverted for the *Seizure* state in Figure 4.b (second row). In fact, the state-wise average FC (left colormap) is overall characterised by higher values out-of-diagonal as well, not surprisingly indicative or a more global and network-widespread synchronization during the seizure. Looking at the allegiance matrix, although persistently coordinated regions are still evidently present, especially in the top left corner of the matrix, there are fewer of these persistently coordinated pairs. Baseline state for the considered subject is associated to a marked distinction between regions that tend to be grouped together (red blocks in allegiance matrix) and regions that tend to be grouped apart (blue stripes), associated to a reconfiguration of within module connectivity. In the seizure state, blue is dominant for this patient. Module identity is not as sharply maintained as in baseline, despite speed is substantially reduced. Thus a fast module-respecting dynamics at baseline is replaced by a slower module-mixing reconfiguration flow during the Seizure. Note that modularity during the Seizure state is substantially reduced (see Figure 3), so that the reduced allegiance may be associated to a randomness of modular partition extraction in network frames which are not really modular.

The average FC of the third state (third row) in Figure 4.b has a block of persistently connected regions in the top-left corner, that are also connected to two smaller blocks that are visible along the diagonal. The average allegiance matrix of the third state, which we call a *Recovery* state, is characterised by few groups of nodes with high allegiance in its top left part: the matrix elements with higher values in this portion of the matrix correspond to the regions that are most connected in the FC matrix. We note the resemblance of this part of the allegiance matrix to that of the *Seizure* state. The rest of the allegiance matrix appears to be more "crystallized", in analogy with the corresponding part of the same matrix in the baseline state. We can therefore interpret this state as a transitional state, in terms of allegiance and connectivity, between the seizure and the baseline states. This is confirmed also in the density plot of v_t on the right, where the peak of the distribution lies between the two peaks of the same plots in the baseline and seizure states.

Both the FC and the allegiance matrices for the fourth state are different from the previous ones. In the bottom row of Figure 4.b, in the FC matrix (left colormap), we note a separation into two subgraphs (a smaller block in the top left corner of the FC matrix, and a larger block in the bottom right corner) of the 40Hz layer of the network. The same tendency is underlined also in the allegiance matrix ($MA(i, j)$ colormap), where the two separate diagonal blocks of the matrix correspond to two subsets of electrode contacts that move across the different modules in time in a coordinated manner

with other contacts in the same subset, but independently from contacts of the other subset. In other words, this state seems to be characterised by the emergence of two independent "cristal-like" allegiance dynamics of two large groups of regions. Interestingly the two subnetworks, correspond to temporal regions (top left block in the allegiance matrix) and frontal and parietal regions (bottom right block). In the density plot of v_t on the bottom we see how the peak of the distribution of values of v_t is lower than that of the previous state shown in Figure 4.b, which suggests how these state could represent a transient slowing down of the overall connectivity dynamics, where the allegiance is momentarily restricted in a configuration which substantially differs both from the Baseline and the Seizure sates, but also the previous Recovery state. We call for now this state a *"Recovery II"* state, observing, that, depending on the analyzed recording, at least two and, sometimes, even more allegiance states can alternate during the very long post-ictal period.

The analyses of Figure 5.a provide a more direct and precise visualization of the dynamics of alternation between the four allegiance states we just described. In Figure 5.a, we plot the average value of $\langle v_t \rangle_w$ computed over each time window, and we mark each point with a color corresponding to the allegiance state to which it is assigned (the cluster to which it belongs). This analysis confirms and manifest more transparently how the baseline state is actually the state characterised by a faster dynamics, in terms of changes in the connectivity (as already shown in Figure 4.b). Analogously, it becomes also visually evident that the seizure state has the lowest values of $\langle v_t \rangle_w$, at seizure onset and for the following seconds, except for two pre-ictal transient epochs, associated with pre-ictal spike events annotated by the clinicians that occur at baseline and another highly perturbed period of the 40Hz layer occurring between 480 and 840 seconds from seizure onset. The two other Recovery and Recovery II states clearly alternate each other, with the former occurring in moments of increasing dynamics, whereas the latter is present in the sudden drops of dFC speed. Intriguingly, these episodes of sudden dFC speed decreases associated to entering the Recovery II state tend to occur in the proximity of transient language dysfunction markers annotated by the clinician. This observation suggests that the fourth state could be systematically associated with the emergence of aphasia symptoms and that, speculatively, aphasia could be the *consequence* of altered information exchange during the slow and crystallized Recovery II state (see *Discussion*).

2.5 Allegiance state dynamics correlates with transient aphasia

The FC and MA matrices shown in Figure 4.b correspond to archetypes of the clusters of windows associated to each different allegiance state. However, each window corresponds to a different

network reconfiguration snippet with different detailed network frames and sequential arrangements. To correlate allegiance dynamics with symptom occurrence, it is appropriate to develop a soft classification scheme, through which every individual window can be assigned not only a single crisp allegiance state label —fully ignoring window variability and specificity— but, more precisely, a vector of similarities to the different reference allegiance state. We thus introduce a machine-learning classification procedure through which we can estimate the probabilities that each specific window is assigned to each one of the reference allegiance states. Specifically we train a K-nearest-neighbour classifier associating window specific dA matrices with labels obtained by the spectral clustering (see *Materials and Methods*). The probabilities provided as output by the multi-class classifier may peak for specific states at specific times, in correspondence with epochs strongly representative of the state to which they are assigned. However, they could also assume intermediate values comparable for different states, in occasion of smooth transitions or of windows with highly atypical transient frames and flow styles. The systematic increase of the probability of belonging to a given allegiance state in relation to the reporting of language dysfunction could be taken as an indication that this state is indeed functionally related to the emergence of aphasia symptoms.

We show in Figure 5.b the probabilities of belonging to each of the four allegiance states for the same representative recording of Figure 5.a. The magenta curve in Figure 5.b, at the top, corresponds to the probability (value between 0 and 1) of each window, and corresponding allegiance matrix, to be labeled as *Baseline*. We note how the curve is initially close to 1, except for the two previously mentioned sudden drops, and then drops to 0 in proximity of the seizure onset marker, to resume high values only in the last ~ 4 minutes of the recording. On the contrary, the Seizure state's probability curve (in green) starts off with null values, has two sudden peaks corresponding to the drops in the baseline's curve (confirming our intuition that these two episodes may correspond to preictal spikes), and reaches its maximum in the period between seizure onset and the first appearance of aphasia. The rest of the curve undergoes sharp transitions from 0 or low values to higher values, and eventually goes persistently to zero when the baseline curve returns to persistently high values, i.e, when the 40Hz layer of the network returns to its initial regime. The third curve for the *Recovery* state reaches values close to one only starting in the vicinity of the first marker of language dysfunctions, where the Seizure state probability also drops for the first time after the seizure event. The curve then undergoes frequent and sharp binary-like transitions from values close to 1 to values close to 0 until 540 seconds from seizure onset, where the values of the curve peaks begin decreasing more gradually to then persistently remain and near-zero values. The fourth, *"Recovery II"* state is evidently the

rarest, as the peaks of the dark blue curve at the bottom of Figure 5.b are evident but infrequent. Yet they occur in the very proximity of the last three clinical markers (as well as in other later moments up to 860 seconds from seizure onset, well after the ending of symptom follow-up by the clinician). The probability of being labeled as belonging to this fourth state drops to zero only when Baseline is finally recovered.

Visual inspection suggests thus that matching drops in dFC speed (Figure 5.a) and peaks in the probability of being labeled as an epoch typical of the *"Recovery II"* state co-occur with the reporting of aphasia symmptoms. Is this visual impression justified? To rigorously probe this hypothesis, we compute in Figure 5.c a lagged cross-correlation between the probabilities of assignement to each of the allegiance states and the train of aphasia symptoms annotations. To detect significant cross-correlations we check for the existence of cross-correlogram peaks beyond a chance-level band (shaded area) obtained by randomizing the positions of symptom markers (see *Materials and Methods*). From the plots in Figure 5.c we see how only the Seizure state and, especially, the "Recovery II" state have a significant value of correlation with the occurrence of clinical markers. We can summarize this information in a *symptom relation index* Θ, which measures the integrated area comprised between the measured cross-correlation $XC(\tau)$ and the 95% confidence interval (see *Materials and Methods*). In this case, the only two allegiance states with $\Theta > 0$ are the Seizure state with $\Theta = 0.1256$ and the Recovery II state with $\Theta = 0.3231$. The visual impression is thus confirmed through a quantitative statistical indicator.

Table 2. Brain areas per block during Recovey 2 state, Patient 1

Block 1	Counts b.1	Block 2	Counts b.2
Inferior Temporal Gyrus, anterior division	1	Cingulate Gyrus, posterior division	3
Inferior Temporal Gyrus, posterior division	8	Frontal Orbital Cortex	4
Inferior Temporal Gyrus, temporooccipital part	3	Frontal Pole	3
Insular Cortex	2	Inferior Frontal Gyrus, pars opercularis	1
Lingual Gyrus	3	Inferior Temporal Gyrus, anterior division	6
Middle Temporal Gyrus, anterior division	4	Inferior Temporal Gyrus, posterior division	13
Middle Temporal Gyrus, posterior division	8	Insular Cortex	5
Parahippocampal Gyrus, anterior division	7	Middle Frontal Gyrus	2
Parahippocampal Gyrus, posterior division	3	Middle Temporal Gyrus, posterior division	1
Planum Polare	2	Middle Temporal Gyrus, temporooccipital part	4
Superior Temporal Gyrus, posterior division	2	Precuneous Cortex	1
Temporal Fusiform Cortex, posterior division	7	Temporal Fusiform Cortex, anterior division	4
Temporal Occipital Fusiform Cortex	3	Temporal Fusiform Cortex, posterior division	5
Temporal Pole	10		

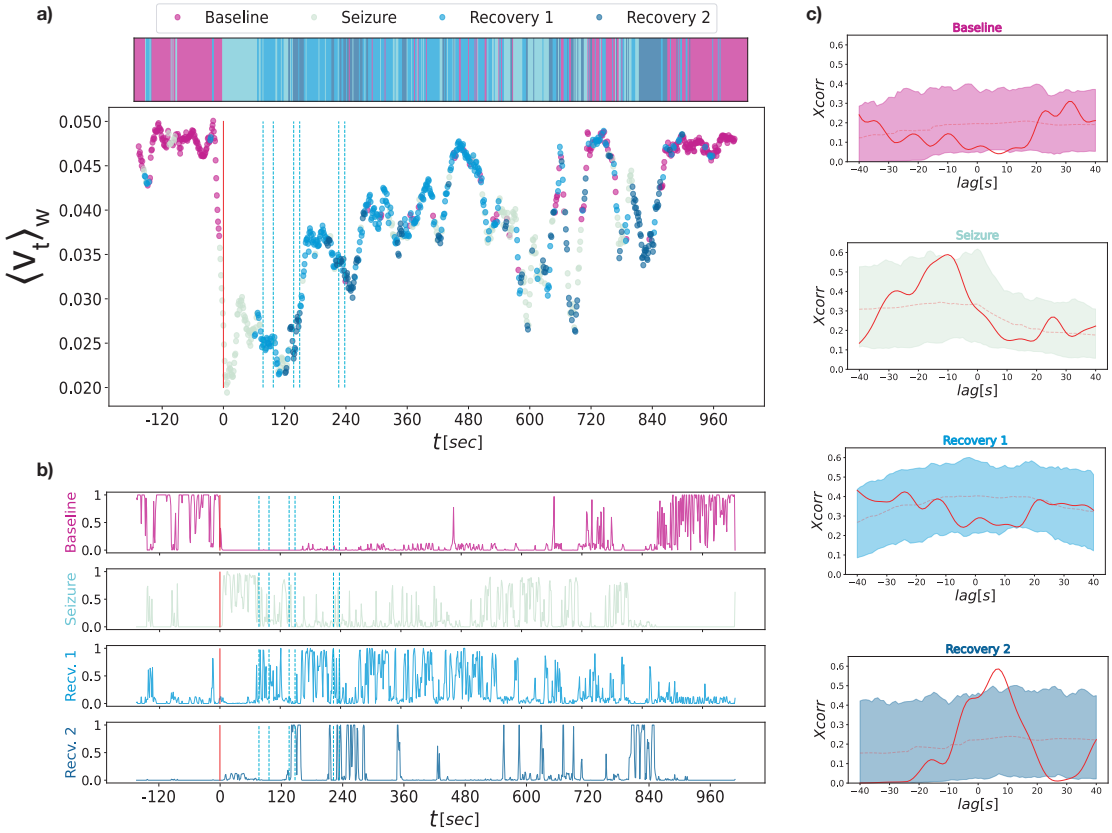

Figure 5. State-wise FC-speed and symptom-relation: a) each dot in the plot corresponds to the average FC-speed value within a time window, colored with the color of the corresponding allegiance state - here it is evident that the baseline state (magenta points at the begginning and end of the recording) is characterised by higher values of FC-speed, whereas the seizure state has the lowest values, hinting at a sudden slowing down of the overall network dynamic reconfiguration; recovery 1 points are concentrated in periods of rising FC-speed and on local maxima, whereas recovery 2 time windows happen around momentary slwoing downs of the dynamics and local minima. Each of the four curves in **b)** represent the probability $P(t) \in [0, 1]$ of each time window t to belong to the baseline (magenta, top), seizure (light green, second plot), recovery-1 (light blue, $3rd$ plot) or recovery-2 (dark blue, bottom) states. Each of the four plots in **c)** represents the lagged cross-correlation between the peaks of the curves in **b)** of each state (baseline, seizure, recovery-1 and recovery-2) with the language dysfunction markers (red line); the shaded areas are comprised between the 5th and 95th percentiles of the values of cross-correlation computed for the peaks of $P(t)$ of each state with a random permutation of the clinical markers in the $[60s, 260s]$ interval.

2.6 Interlayer co-allegiance

We have so far analysed each network layer, or frequency band, independently from each other. What are the inter-relations between their respective dynamics? To answer to this question, we compare the module allegiance dynamics in the different frequency layers, studying whether pairs of electrode contacts switch across time-dependent modules with similar coordination patterns in different layers. To do so, we compute cosine similarity between the allegiance matrix computed in a time window in

Table 3. Brain areas per block during Recovey 2 state, Patient 2

Block 1	Counts b.1	Block 2	Counts b.2
Inferior Temporal Gyrus, posterior division	5	Frontal Operculum Cortex	5
Middle Temporal Gyrus, anterior division	10	Frontal Orbital Cortex	5
Middle Temporal Gyrus, posterior division	16	Frontal Pole	34
Parahippocampal Gyrus, posterior division	1	Inferior Frontal Gyrus, pars opercularis	6
Planum Polare	2	Inferior Frontal Gyrus, pars triangularis	2
Superior Temporal Gyrus, anterior division	3	Insular Cortex	1
Temporal Fusiform Cortex, posterior division	4	Middle Frontal Gyrus	5
Temporal Pole	17	Middle Temporal Gyrus, anterior division	7
		Parahippocampal Gyrus, anterior division	5
		Parahippocampal Gyrus, posterior division	1
		Temporal Fusiform Cortex, anterior division	1
		Temporal Fusiform Cortex, posterior division	2

Table 4. Brain areas per block during Recovey 2 state, Patient 3

Block 1	Counts b.1	Block 2	Counts b.2
Heschl's Gyrus (includes H1 and H2)	4	Inferior Temporal Gyrus, temporooccipital part	2
Insular Cortex	10	Lingual Gyrus	3
Parahippocampal Gyrus, anterior division	4	Middle Temporal Gyrus, temporooccipital part	5
Planum Polare	4	Temporal Occipital Fusiform Cortex	1
Planum Temporale	1		
Superior Temporal Gyrus, anterior division	2		

a layer, with the allegiance matrices computed in the same window for each of the other layers, for all the time windows. We therefore end up with a time series of allegiance similarity for each pair of layers (Figure 6.a): we refer to this measure we introduce as the *multiplex inter-layer coallegiance* A_{mpx} (see *Materials and Methods*).

We first consider the multiplex co-allegiance between the two high frequency layers at 40 and 20 Hz, since they are the ones showing the strongest effects of seizure on network dynamics. This analysis reveals an increase w.r.t. baseline of multiplex allegiance in all the other states (Figure 6.b). On the left, we show detailed time-series of multiplex co-allegiance with window resolution. Both the Seizure and the Recovery II state have distributions of 40-20Hz co-allegiance peaking at increased values, as visible from the time-series frequently having excursions beyond the range of baseline variation (shaded band in Figure 6.b). To better appreciate variations between states, we compute at each window percent variations of co-allegiance relative to the mean co-allegiance in the baseline state. Boxplots of these relative co-allegiance variations, grouped by allegiance states, are shown to the right of Figure 6.b. The box for the baseline state has an average value of zero by construction. The boxes for all the other states are shofted toward positive increases of co-allegiance, more marked for the two states, Seizure and Recovery II showing an association with language dysfunction. Therefore, the dynamic re-organization of network modules in the 40Hz and 20Hz frequency bands become

more similar, and locked, during the seizure allegiance state.

An opposite trend is found for the inter-layer coallegiance of the 40Hz and 10Hz layers. In fact, here the seizure state is characterised by a sensible drop in coallegiance w.r.t. baseline (Figure 6.c, left). The state-wise distributions of coallegiance values of the Seizure, Recovery and Recovery II states are peaked around lower values w.r.t. baseline (Figure 6.c, right), suggesting here that seizure onset induces an increased decoupling between these two layers which is only very slowly re-established through the long recovery phase.

We finally compare the 20Hz and 10Hz frequency bands in Figure 6.d. As for the previous comparison between the 40 and 10Hz layer, seizure initially induces a drop in co-allegiance, at least in this recording (Figure 6.d, left). However, values of co-allegiance become then generally larger, since the Seizure state (not significantly, though) and then even more for the both Recovery and Recovery II states. This is similar to the co-allegiance dynamics between the 40 and the 20Hz layers (Figure 6.b), however the effect is smaller.

To conclude, the network reorganization dynamics in time of the different functional connectivity layers are not independent, but display a clear co-allegiance, i.e. a coordination in which the floating of different network nodes across dynamically forming and reshaping network modules occur. At Baseline, this co-allegiance is weaker between the 40 and the 20Hz layers ($A_{mpx} \approx 0.65$, Figure 6.b, right) and greater with the 10Hz layer ($A_{mpx} \approx 0.75$ between the 40 and the 10Hz layer and between the 20 and the 10Hz layer, Figure 6.c and d, right). However, the onset of the Seizure perturbs this co-allegiance dynamics, increasing its coupling between the fast layers, and reducing the coupling of the 40 with the 10Hz layer. These disruptions are likely to perturb the proper cross-frequency coupling patterns needed for language function (see *Discussion*).

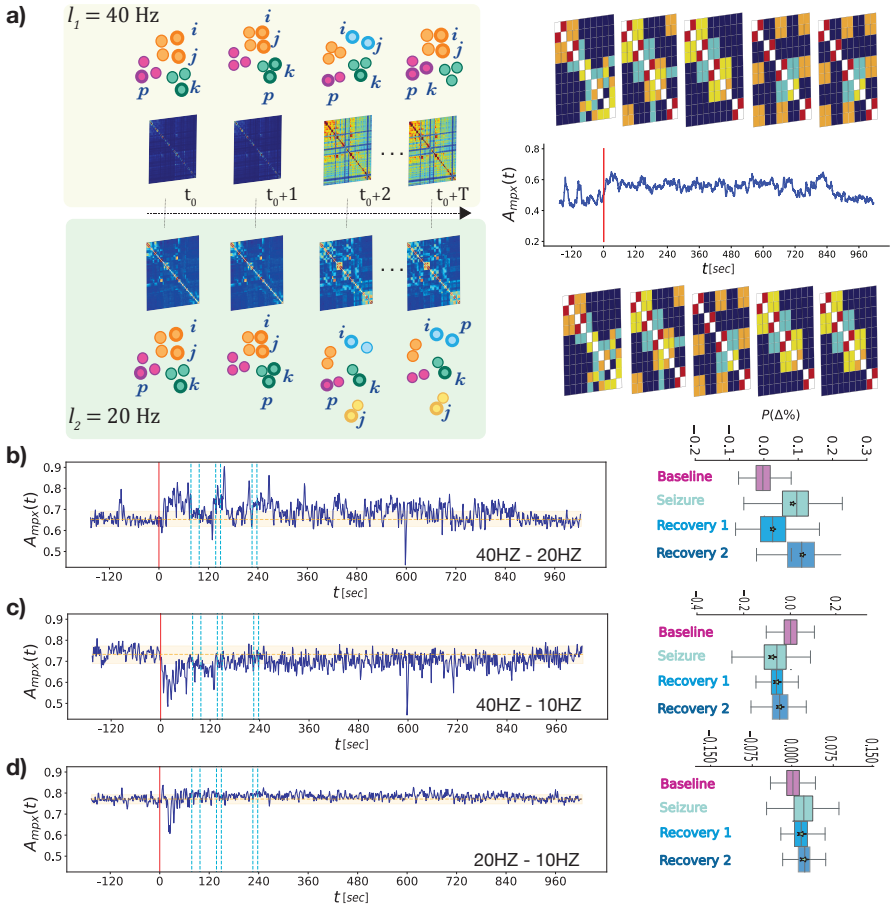

Figure 6. Inter-layer coallegiance: a) For each pair of layers ($l_1 = 40$Hz and $l_2 = 20$Hz in the cartoon on the left) we compare the partition into modules at each time stamp by computing the cosine similarity of the relative module assignments - (right) the instantaneous inter-layer cosine similarity computed between the allegiance matrix of the 40Hz layer in a time window and the allegiance matrix of the 20Hz layer in the same window, recording 1. **b-c-d)** In each figure we plot: on the left, the curve of inter-layer coallegiance (dark blue) and compare it to the average value of inter-layer coallegiance found in the baseline state (orange dotted line, the orange-shaded area corresponds to values between the 5th and 95th percentile of baseline inter-layer coallegiance values); On the right, each box describes the distribution of the inter-layer coallegiance within the corresponding allegiance state (baseline in green, seizure in orange, recovery 1 in blue, recovery 2 in pink). The plots in **b)** correspond to the comparison of the 40Hz and 20Hz frequency bands of the representative recording, **c)** to 40Hz vs. 10Hz frequency bands and **d)** to 20Hz vs 10Hz, where the allegiance states have been retrieve by analysing the 20Hz layer.

2.7 Comparison of different seizure recordings

After presenting all the analyses for a reference recording, we finally turn to comparing results across different recordings and identifying similarities and cases of discordance. While many seizure-related phenomena are consistently observed across all recordings, others show more variability across seizures (see *Discussion* for possible interpretations).

To manifest similarities and differences across different subjects and different recordings, we

graphically represent a compendium of descriptive features for the different allegiance states (columns) of each the considered recordings (rows; the first row reports information for the reference recording, discussed in detail in the preceding figures). Specifically, we display, in the form of radar plots, the following quantities (from the top in clock-wise order):

- the mean value of the dFC-speed $\bar{v}$ within the relative allegiance state;
- the *symptom relation index* Θ;
- mean value of the allegiance matrix computed over all the time points included in the relative allegiance state $\bar{A}$;
- the state-wise average value of the inter-layer co-allegiance computed for the 40Hz and 20Hz layers.

Different recordings on the rows of Figure 7, and the values on the radial axes are normalized in each row, whereas each column corresponds to a different allegiance state. The baseline state is *systematically* characterised by the highest values of $\bar{v}$, suggesting how the baseline activity, in the 40Hz layer, causes a fast reconfiguration of the functional connectivity. This dynamics is on the contrary slowed down the most during the seizure allegiance state, whereas for the two recovery states we note the tendency to have connectivity reconfiguration speeds intermediate between the baseline and the seizure states. For most seizures and patients (all recordings apart from Patient 2 seizure), the speed was faster for the Recovery I state and slower for the Recovery II one. The feature most consistently discriminating the Recovery II states from the other was however their high correlation with the language impairment markers, the largest among all allegiance states in all considered recordings.

The median allegiance strengths $\bar{A}$ also varied across states for all seizures. However, we observed different patterns of variations for the distinct recordings. As previously discussed, for the reference seizure, the baseline state had the largest median allegiance strength and the seizure state the lowest. However for the other recordings, including a second seizure for the same Patient 1, the opposite occurs, with the baseline state having the lowest median allegiance strength and the seizure state a much larger value. Therefore, the onset of seizure can impact on the degree of internal ordering of module reconfiguration dynamics in two ways: dissolving baseline spatio-temporal organization when it exists, or, on the contrary, freezing modules when they evolve with great freedom at baseline. In both cases, the recovery state show values in intermediate ranges, gradually increasing or decreasing toward the baseline values observed prior to the seizure.

Analogously, the median allegiance strength between the 40Hz and the 20Hz layers also display clear variations between baseline and the other states, but not always in the same direction for all seizures. In three out four of the considered seizure recordings, inter-layer allegiance is weak at baseline and strong during seizure, to then gradually decrease toward baseline values in the Recovery I state. However, the situation is different for one seizure recording in Patient 3 (last row in Figure 7) for which baseline inter-layer allegiance is strong and drops in the seizure state.

To conclude, allegiance states across the different seizure recordings have important qualitative similarities, but also some differences, that our methods for comparing network dynamic reconfiguration flows are able to pinpoint. Importantly, in all seizures, network dynamics at baseline and during seizure are radically different in style, with Recovery states displaying transitional properties. One possible reason for the discrepancies in the direction of feature changes may be that the baseline state is in reality not unique but heterogenous in nature. Thus, different seizures (within a given subject or across different subjects) may be associated to different types of network dynamics alterations depending on the specific baseline condition in which the seizure is triggered (see *Discussion*).

Table 5. Absolute values of the features displayed in Figure 7 for all recordings.

Patient 1 rec. 1	State	$\bar{v}$	Θ	$\bar{A}$	ILC_{20Hz}^{40Hz}	ILC_{10Hz}^{40Hz}	ILC_{10Hz}^{20Hz}
	Baseline	0.048427	0.000000	0.269140	0.652322	0.732896	0.771437
	Seizure	0.029320	0.130109	0.075238	0.706959	0.676124	0.780425
	Recovery 1	0.040629	0.000000	0.109371	0.668743	0.690736	0.783780
	Recovery 2	0.032766	0.579639	0.147182	0.725582	0.700006	0.787612
Patient 1 rec. 2							
	Baseline	0.003530	0.000000	0.221519	0.702906	0.766885	0.822679
	Seizure	0.000779	0.000000	0.348581	0.812069	0.886870	0.825763
	Recovery 1	0.002115	-0.005870	0.170053	0.772118	0.796673	0.829347
	Recovery 2	0.001146	0.189989	0.205292	0.763039	0.774996	0.825457
Patient 2							
	Baseline	0.027833	0.000000	0.061227	0.805935	0.684796	0.811552
	Seizure	0.016485	0.134928	0.167022	0.828347	0.741896	0.850336
	Recovery 1	0.023148	0.000000	0.210452	0.843399	0.769216	0.827033
	Recovery 2	0.026493	0.907741	0.099023	0.843395	0.800636	0.828520
Patient 3							
	Baseline	0.035345	0.096972	0.085706	0.756283	0.685543	0.844199
	Seizure	0.027083	0.000000	0.098120	0.728054	0.670637	0.771065
	Recovery 1	0.030225	0.000000	0.120874	0.698316	0.641979	0.834501
	Recovery 2	0.029053	0.239141	0.103834	0.737310	0.683400	0.836820

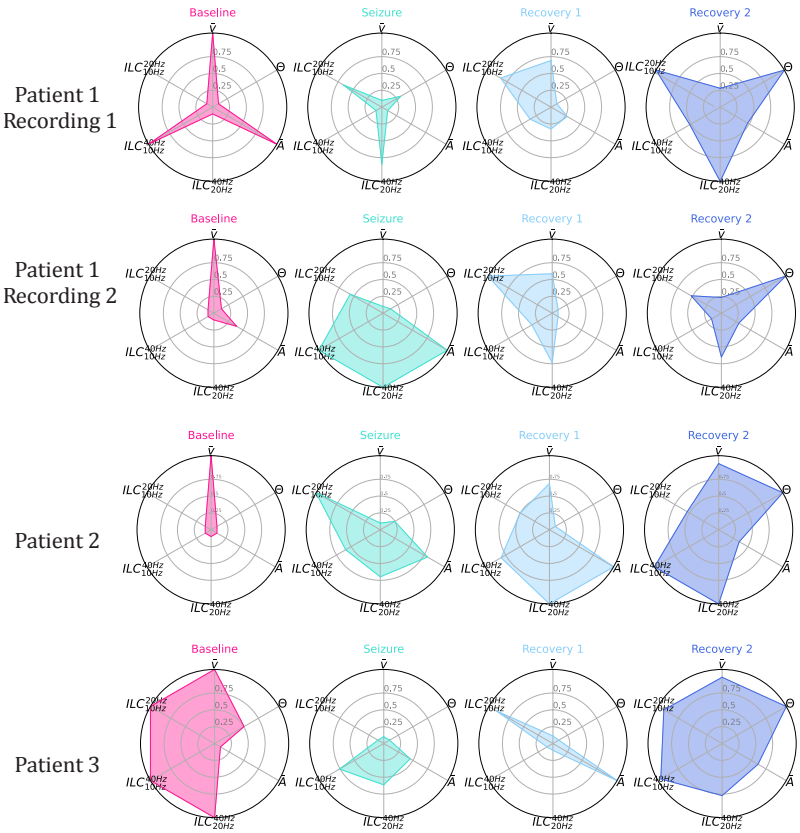

Figure 7. Allegiance states in the 40 Hz band: for each recording (two recordings of patient 1 and one recording each for patients 2 and 3) we show here four allegiance states by plotting on a radar plot four quantities: (from the top, clock-wise) the FC-speed averaged on the time points of the corresponding state; the Θ index of each state; the average over the allegiance matrix computed on the time points assigned to the relative state; the average inter-layer coallegiance computed over the corresponding allegiance states between the 40Hz and 20Hz layers. The four quantities that give rise to each of the four radar plots of a recording are normalised over the recording: a value of 1 of a quantity in a radar plot means maximum value of that quantity with respect to radar plots in the same row. The magenta radar-plots correspond to the baseline state; the light green plots correspond to seizure states, light and dark blue plots correspond to recovery 1 and 2, respectively.

3 Discussion

In this work, we introduce a new approach to study multi-frequency time-varying data as a temporal multiplex network: such temporal multiplex approach is relatively new and few studies have started using it in a more computational framework [27], while no other data-driven studies with applications in systems neuroscience can be found in the literature.

Our paradigm of analysis could be applied to very general types of neural signals —e.g. dFC from multimodal EEG/fMRI recordings [1]— and to non-neural signals as well, as long as a temporal multiplex network representation is pertinent for them. Here we apply our approach to electrophysiological data deriving from intracranial recordings in epileptic patients. Doing so, we are in

line with previous studies that also observed the importance of accounting for functional network dynamics in describing and controlling the evolution of brain activity along seizures. These studies however focused only on slow fMRI signals [21] or uniquely on the high-gamma component of the intracranial EEG signal [41], thus integrating a temporal but not a multiplex dimension. In our study, the different time-evolving layers of the temporal multiplex correspond to coherence between brain regions in a different frequency bands. Coherence between neuronal populations is generally seen as a mechanism allowing information exchange and routing [19] and communication-through-coherence can occur simultaneously at multiple frequencies, thus providing a way to open different parallel information channels [8, 31]. A multiplicity of frequencies could also enable the routing of neural representations stored and processed at different time-scales [11]. Therefore, a temporal multiplex description of multi-channel neural activity recordings is naturally and particularly fit to capture the complexity of flexible information routing.

In the specific case of language-related processing, different frequencies may be exploited to pace the neural parsing of different language elements of different typical durations, as phonemes, syllables, words, sentences form sequences with different nested time-scales [20, 30]. Language production and understanding requires thus the correct and flexible integration of all these language elements. If we think that functional network dynamics is a proxy for dynamic information processing [13, 23, 36, 37], then we expect that the dynamics of coherence networks at different frequencies should display some optimal level of coordination, neither completely independent (as the processing of, e.g., words is affected by the processing of syllables, etc.), nor completely synchronized (as every language level must be processed with specific rules). Correspondingly, we find that baseline inter-layer allegiance values are far from zero, indicating inter-frequency dynamic coordination, but also below one (Figure 6b). Seizure onset increases the mutual enslavement of network dynamics int the 40Hz and 20Hz layers, thus potentially perturbing the fine hierarchical coordination of information processing which underlies language function.

Besides generalizing temporal graph methods from single- to multi-layered networks, we introduce here qualitatively new approaches for studying not only the variation along time of instantaneous network frames but, also, the variation of their flow of reconfiguration. Indeed, adopting a double time-scale, we can monitor whether the dynamical properties of the network reconfiguration flows on the faster time-scale are evolving at different observation windows at the slower time-scale. In other words, we don't compare networks, we compare network dynamics. An instrumental notion to do so is the one of allegiance states, accounting for the properties of dynamics within each state, unlike

more convention dynamic Functional Connectivity (dFC) states which still describe static properties of state-averaged networks [2]. We trace a variety of discrete states of flow for each of the layers of the multiplex: these allegiance states represent different dynamical styles of the nodes of the network to float across the different communities/modules of the network, in more or less coordinated or random manners. The dynamical nature of these states is highlighted by the speed feature, whose non-zero value indicate that faster or slower network reconfiguration events are continually occurring within each allegiance state epoch. It is precisely this speed feature —akin to quantities previously introduced to characterize dFC in resting state fMRI recordings [9, 28]— that better allows to identify similar allegiance states across different recordings and patients.

Eventually, we note that the allegiance state which we called "Baseline", as preceding the seizure event in the considered recordings, does not correspond to some optimal functional connectivity architecture that would then be broken when entering into the pathological Seizure state. Quite on the contrary, for all considered recordings, the baseline states were associated to the highest values of network reconfiguration speed. The speed of network dynamics then dramatically slows down when entering the Seizure allegiance state, as an effect of the activity hyper-synchronization, and only slowly grows back to normal baseline values through the different Recovery states (Figure 4). Thus, prior to seizure, "healthy" baseline is a condition of steadily flowing network dynamics.

Measuring speed is however not enough to fully characterize the style of network reconfiguration. The allegiance matrix block structure and values tell which network nodes co-switch across network modules along the network reconfiguration flow and which others on the contrary tend to swap modules independently from each other. For some patient- and recording-specific states, the allegiance matrix is rather structured. This is the case for instance of the baseline state for the first seizure recording of patient 1 (top row in Figure **??**) or for the Seizure state of the second seizure recording of the same patient (second row of Figure **??**). These similar values of average allegiance strength correspond however to very different conditions. In high-allegiance baseline states, networks are strongly modular at any time and evolve at high speed, while during the Seizure state network connectivity is frozen into configurations whose community structure is much less clear. The high allegiance of Seizure (and Recovery) states may thus just indicate the existence of correlated noise in the fluctuating neighborhoods of different network nodes. On the contrary, the coexistence of high allegiance and high speed at baseline denotes the existence of a network flow with a complex spatio-temporal organization between order and disorder, speculatively associated to boosted potential for computation [15].

The question then naturally arises of why baseline states for the different recordings have so different values of average allegiance strength (see Table 5). We don't have a conclusive answer to this question and we can only speculate about possible reasons. First, seizures can occur at different times, when patients are resting or differently active, and thus potentially in cognitively different states associated to higher or lower information processing work-loads. Second, not all seizures are identical. Even abstracting from differences in clinical and aetiological conditions, purely mathematical analyses identify alternative pathways for the transition from a non-epileptic to seizure onset and then offset [22, 40]. These different universal scenarios ("dynamotypes") may lead to different network dynamics fingerprints and thus different patterns of dFC found in different seizures could match different seizure onset and offset mechanisms. Finally, another more prosaic explanation could be linked to the specific contingencies of recording acquisition in a real-life, research-suboptimal clinical environment. The lengths of the baseline period prior to seizure are different in the different recordings. For instance, in the first seizure recording for patient 1, we could observe a substantial period of baseline prior to seizure, and also confidently converge back to a new baseline condition after the long recovery period. In the second seizure recording for patient 1 and for the other two patients, the observed baseline period was much shorter. In the case of patient 3, it is likely that the recording was stopped before having completely restored to a baseline condition. These details can reduce the quality of allegiance state identification and segmentation as a reduced number of observations may lead to the spurious attribution to the baseline cluster of time-windows which are in reality already contaminated by pathology-related activity. The distinctions between states would thus be blurred. Analyses of a much larger number of seizures would be required to clarify the origin of baseline and allegiance states differences across different patients. Yet, it is positive that our analysis paradigm is able to identify subtle qualitative inter-state differences of dynamical style, going beyond rough distinctions between pre-, during- and post-seizure stages. More remarkably, our analyses have the power to identify patient-specific differences, which is a necessary pre-requisite to yield neuromarkers for personalized diagnosis and prognosis.

Another robust result of our analyses is the existence of not just one but more Recovery states. These recovery states have properties interpolating between baseline and Seizure allegiance states. The Recovery I state is observed over time ranges lasting well beyond the last markers of language dysfunction annotated by the clinicians.

The Recovery I state also is the state through which network dynamics gradually "gears up" toward the high-speed of reconfiguration associated to baseline. On the contrary, the Recovery

II state, in three out of four considered seizures, correspond to transient slowing down of speed, interrupting the speed ramping up (only for patient 2 seizure, the two Recovery states have similar speed levels). Specifically, the Recovery II state tend to occur in local minima of the FC-speed, and correspond to moments in which the network is transiently "trapped" in a dysfunctional regime with substantial differences in network dynamics when compared to the other states. Indeed, the allegiance matrix in the Recovery II states is split into two independent sub-networks, such that nodes in a subnetwork float across dynamically changing network modules in a coordinated manner, but independently from fluctuations of nodes in the other subnetwork. Importantly, one of the sub-networks includes mainly temporal brain regions, whereas the other is mainly composed of frontal and parietal regions (see Tables **??**). As an effect of this compartmentalization of the allegiance matrix, temporal and frontoparietal nodes become functionally segregated, while proper language function requires their communication. Given the peculiar functional organization of network flow within the Recovery II state, it is perhaps thus not surprising that the occurrence of this state correlates with the reporting of aphasia symptoms, as denoted by the systematically large values of the Θ index: the perturbed spatiotemporal organization of dFC during the Recovery II state is indeed particularly harmful to information processing within the distributed language system, whose loss of internal integration could *causally* induce language dysfunction.

The effects of Seizure on dFC are more prominent in the 40Hz layer than in other layers. While the dynamics of the 20Hz layer is qualitatively similar to the one of the 40Hz one, for slower frequencies, dFC is almost unchanged across the preictal, ictal and postictal periods. Furthermore, seizure-related variations of dFC are more evident when analyzing unipolar time-series of activity (single electrode contacts), rather than functional connectivity derived from the most commonly used bipolar time-series (difference of neighboring electrode contacts, cf. SUpplementary Figure S3). These results may seem surprising, as the intracranial sEEG power at high frequency is much weaker than at slower frequencies and unipolar signals are usually considered to be heavily flawed by volume conduction. However, power in the medium-to-high gamma range has been shown to be correlated with modulations of firing rate synchrony at the population level [33, 39]. It is thus possible that the richer dynamics of the 40Hz layer reflect indirectly dynamic patterns of correlated firing, such as neural avalanches [10], propagating volleys of activity [24] or transient coherence bursts [34]. For this same reason, unipolar time-series could be more informative than bipolar time-series. Indeed collective activity is not generated locally, but simultaneously occurs and is co-generated over distributed circuits. Therefore, neighboring electrodes may be capturing similar patterns of collective

activity and this shared component would not be noise to remove (as in bipolar montages) but rather informative signal to retain (as in unipolar time-series).

It is possible that the weak level of seizure-related modulations we observed in the low frequency layers is due to methodological limitations. With our methods of network construction, connectivity in the layers at lower frequencies is less modular and more global (cf. Supplementary Figures S3-S4). In the future, the extraction of dynamics in low frequency layers could be potentially improved by the adoption of broader and subject-specific bands of analysis, as well as of specific significance thresholds for each individual layer of edges in the temporal multiplex, thus assuring the same density in each layer.

Another limitation of our study is the poor attention devoted so far to spatial details. Our analysis paradigm provide a very rich characterization of the style of network reconfiguration through time (faster or slower, more or less organized), however, considering spatial structure, we insist mostly on global properties (as the overall degree of modularity or total connectivity strength). Understanding the relation between altered network states and pathological dysfunction, requires entering more in the detail of network nodes whose connectivity is the most affected, as the different recorded regions are not functionally equivalent. Here, as a first step on this direction, we have started investigating the existence of a fronto-parietal vs temporal split in Allegiance states linked to the reporting of aphasia symptoms. However, a greater level of detail could be achieved. A possible compromise between incorporating greater spatial information, while still emphasizing the dimension of temporal change could come from the use of meta-connectivity or edge-centric connectivity approaches [16, 28], which allow identifying hubs of importance not because they are strongly connected on average but because they orchestrate the coordination of many dynamically changing links. Reaching this greater level of detail, however, would be facilitated once again by the analysis of a greater number of recordings, which would better allow stratifying the great diversity of epileptic dynamics across different patients.

In conclusion, in this work we use a data-driven, temporal networks approach, through which we find that not only the transient configurations of FC can represent a meaningful observable that relates to brain state and health condition changes, but also the type of dynamical regime itself, characterized in terms of its internal features of network reconfiguration style. Different allegiance states are characterised by clearly different values of the rate of change of the FC, the dFC-speed, which in turn suggests that we are not dealing with a set of different "frozen" structures, but that each state could instead be seen as a different way of the system to explore the ensemble of the

possible configurations of FCs. The rate of the variability of the temporal network itself is what we conceive as the fundamental criterion to identify an allegiance-state: this variability can resemble the motion of a very viscous substance, as we see in the Seizure state, where the overall dynamics is slowed down; or it could be more like the motion of free particles in a gas or a flowing liquid stream, as is the case in the baseline allegiance states, which have faster dynamics and varying degrees of internal order. Thus network dynamics is not noise on top of static functional architectures but a functional mechanism by itself (what matters is not only how networks are but also how networks change): this implies that alterations of dynamics may lead to dysfunction. This is what we start finding evidence for, with this work, where two of the identified allegiance states coincide with the language impairments of aphasic epileptic patients. This evidence opens promising avenues for the design of novel, sensitive biomarkers that capture the different dynamical styles displayed by brain networks during their evolution, in both healthy and unhealthy conditions. This goal will be achieved only by crafting the right tools to describe not only the spatial organization of networks but also the spatiotemporal organization of their flow of reconfiguration.

4 Methods

4.1 Recordings

The SEEG recordings were performed using intracerebral multiple contact electrodes (10 to 15 contacts, length: 2 mm, diameter: 0.8 mm, 1.5 mm apart from edge to edge) implanted according to Talairach's stereotactic method [3]. The strategy of electrode positioning was established in each patient based upon hypotheses concerning the localization of the epileptogenic zone (EZ), with the aim of defining subsequent cortectomy. These hypotheses of the likely EZ localization were based on noninvasive presurgical assessment including detailed clinical history, surface video-electroencephalographic (EEG) recording, MRI, and 18FDG-PET scanner. Electrode positions were therefore not standardized across the present series, but were chosen according to the individual clinical characteristics of each case. However, electrode coverage in all cases included at least several cortical contacts being parts of the language network: i.e., temporal lateral and basal temporal region, inferior frontal gyrus, anterior part of the insula [38]. Implantations were unilateral or bilateral depending on the individual features of each case. Signals were recorded using a 256-channel Deltamed system, at a 1024-Hz sampling frequency.

4.2 Wavelet coherence

In order to compute the wavelet coherence between each pair of signals, and thus construct a graph representation of the data, we decompose signals in the time-frequency domain along the Morlet wavelet family. The Morlet wavelet is defined for frequency f and time τ as:

$$\Psi_{\tau,f}(u) = \sqrt{f} e^{i2\pi f(u-\tau)} exp\left(-\frac{(u-\tau)^2}{\sigma^2}\right), \tag{1}$$

so that $\Psi_{\tau,f}(u)$ is the product of a sinusoidal wave at frequency f with a Gaussian function centered at time τ, with a standard deviation σ proportional to $1/f$. The wavelet transform of a signal $x(u)$ is a function of time τ and frequency f given by the convolution with the Morlet wavelet:

$$W_x(\tau, f) = \int_{-\infty}^{+\infty} x(u) \cdot \Psi^*_{\tau,f}(u) du. \tag{2}$$

From the wavelet transform of two signals x and y, we can define the wavelet cross-spectrum between x and y around time t and frequency f:

$$SW_{xy}(t, f) = \int_{t-\delta/2}^{t+\delta/2} W_x(\tau, f) \cdot W^*_y(\tau, f) d\tau \tag{3}$$

where δ is a scalar that depends on the frequency. The wavelet coherence $W.C.(t, f)$ is defined at time t and frequency f by:

$$W.C.(t, f) = \frac{|SW_{xy}(t, f)|}{[SW_{xx}(t, f) \cdot SW_{yy}(t, f)]^{1/2}} \tag{4}$$

where $W.C.(t, f)$ has values between 0 and 1. We compute the wavelet coherence $W.C(t, f)$ for each pair of signals in 5 frequency bands peaked around 1Hz, 5Hz, 10Hz, 20Hz and 40Hz, where the width of the time integration $\delta = 6/f$, and thus the width of each of the frequency bands equals 1/6 of the peak frequency. We define a significance threshold for the coherence values by computing the coherence for pairs of randomly generated oscillating signals (500 iterations), and thus consider as significant values measured on empirical data only those that lie above the 95% confidence interval of the distribution of coherence of the random data. The sampling frequency of the recording is 1024Hz, and we down-sample the time series of the coherence between each pair of signals by a factor 12, with a resulting time resolution of each layer of the temporal-multiplex of $\tau = \frac{12}{1024}$s.

4.3 Dynamic allegiance states

Several approaches have been developed to detect the presence of densely interconnected communities in temporal networks. In this work, given the size and complexity of the data we analyse, we focus, rather then on retrieving purely *temporal* communities, on investigating the mutual relations among nodes with respect to their instantaneous (static, computed at each time stamp) community memberships. In particular, we retrieve the instantaneous partition of the network on each of its snapshots and then compute, within a desired time window, the probability of each pair of nodes to be found in the same community at the same time.

4.3.1 Allegiance

We do so detecting the instantaneous community partitions by a modularity based approach (the Louvain algorithm, **(author?)** [12]), and, within a time window w of 200 time points (~ 2.34 seconds), we compute the so called *module-allegiance*, or *association* matrix [7] T^w_{ij}, whose matrix element corresponds to the probability

$$T^w_{ij} = \sum_{t \in w} \frac{\delta(c^i(t), c^j(t))}{|w|},$$

where $c^i(t)$ and $c^j(t)$ are the communities of nodes i and j at time t, respectively, and $|w|$ is the length of the time window w. We then slide the time window by a lag $\tau = 100$ pts. ($\tau = 1.171$ seconds), and compute the allegiance in the next window. Consecutive windows have therefore a 50% overlap in time.

4.3.2 Dynamic Allegiance

The layer-wise Dynamic Allegiance, dA^l, shown in Figure 4 for the 40Hz frequency band, is obtained by computing the cosine similarity between the upper triangular part (linearized into an $N * N - 1/2$ vector $V^l(t)$) each allegiance matrix computed in the window $t^* \in [L_w, L_w + \tau, \ldots, T/\tau]$ (where τ is the 100 time points lag by which we slide the time window) and all of the other allegiance matrices,i.e. :

$$dA^l(t, t^*) = \frac{\sum_{a=1}^{N(N-1)/2} V^l(a,t) V^l(a,t^*)}{\sqrt{\sum_{a=1}^{N(N-1)/2} V^l(a,t)^2} \sqrt{\sum_{b=1}^{N(N-1)/2} V^l(b,t^*)^2}} \tag{5}$$

The matrix element $dA^l(t, t*)$ therefore ranges from 0, when the two allegiance matrices in windows t and t^* are completely different, to 1, when the two are exactly identical. The block-wise structure of a layer's dA suggests the existence of epochs, or states, in which the allegiance matrices computed

in the corresponding time windows are similar: these are states in which the allegiance dynamics of nodes (brain regions) is in a stable and persistent regime, that we refer to as *allegiance states*.

4.4 Clustering and KNN classification

4.4.1 Clustering on the dA: allegiance states

In order to extract periods of time (clusters of time windows) characterized by similar module allegiance of nodes, we use a spectral clustering method (implemented in the scikit-learn python library **(author?)** [35]) where the dA matrix serves as the distance metric between time-points. Since the method requires an a-priori choice of the number of clusters, we iterate the clustering for different numbers of clusters, thus selecting the result yielding the maximal silhouette score. The silhouette score of a partition into clusters of a dataset is equal to 1 (maximum) when there is 0 overlap between clusters and all data points have been assigned to the right cluster; it is 0 when there are overlapping clusters and -1 when all data points have been assigned to the wrong cluster.

4.4.2 Unsupervised classification for soft allegiance-state labeling of time-windows

We use the K-nearest-neighbor unsupervised classification method (scikit-learn implementation), trained on the allegiance state labels of all the time windows, to obtain a soft classification of each the latter. This allows us to represent each module allegiance matrix computed in the relative time-window as a (in the case of **Patient 1**, as presented in Figure 5.b) 4-dimensional normalized vector: each component of this vector represents the probability of the time-window to belong to the corresponding allegiance state (Baseline, Seizure, Recovery 1, Recovery 2).

4.5 Symptom relation index Θ

The *symptom relation index* Θ is defined as:

$$\Theta = \sum_{\tau \in \Gamma} XC(\tau) - XC_{shuffled}(\tau), \tag{6}$$

where $\Gamma = \{\tau \| XC(\tau) \geq 95\%_{percentile \quad chance \quad level} \quad XC_{shuffled}(\tau)\}$. Thus Θ corresponds to the area comprised between the measured cross-correlation $XC(\tau)$ and the 95% confidence interval (upper bound of colored area in Figure 5.c).

4.6 dFC-speed

The instantaneous dFC-speed v_t as visually introduced in Figure 2.c (top) is defined as the cosine similarity between the FC matrix at time t and that corresponding to the previous, adjacent time point $t-1$ (linearized into $N*N-1/2$ vectors $FC_{vec}(t)$, $FC_{vec}(t-1)$):

$$v(t,t-1) = \frac{\sum_{a=1}^{N(N-1)/2} FC_{vec}(a,t) FC_{vec}(a,t-1)}{\sqrt{\sum_{a=1}^{N(N-1)/2} FC_{vec}(a,t)^2}\sqrt{\sum_{b=1}^{N(N-1)/2} FC_{vec}(b,t-1)^2}} \tag{7}$$

while the time-window-averaged dFC-speed $\langle v_t \rangle_W$ corresponds to the average value of the instantaneous dFC-speed v_t within a 200 time points ($\sim$ 2.34 seconds) time-window W (the same windows for each of which the module allegiance was computed).

4.7 Interlayer co-allegiance

We define the interlayer co-allegiance between each pair of layers (l, l^*) as the cosine similarity between the allegiance matrix computed in a time window in layer l (specifically, the upper triangular part of the matrix, linearized into an $N*N-1/2$ vector $V^l(t)$), with the allegiance matrix computed in the same window layer l^*, for all the time windows:

$$A_{mpx}^{l,l^*}(t) = \frac{\sum_{a=1}^{N(N-1)/2} V^l(a,t) V^{l^*}(a,t)}{\sqrt{\sum_{a=1}^{N(N-1)/2} V^l(a,t)^2}\sqrt{\sum_{b=1}^{N(N-1)/2} V^{l^*}(b,t)^2}} \tag{8}$$

.

5 Acknowledgements

N.P. has received funding from the European Union's Horizon 2020 research and innovation programme under the Marie Skłodowska-Curie grant agreement No. 713750. Also, the project has been carried out with the financial support of the Regional Council of Provence- Alpes-Côte d'Azur and with the financial support of the A*MIDEX (ANR-11-IDEX-0001-02), funded by the Investissements d'Avenir project funded by the French Government, managed by the French National Research Agency (ANR). D.B. is supported by the European Union Innovative Training Network "i- CONN" (H2020 ITN 859937)

A.B. is supported by the Agence Nationale de la Recherche (ANR) project DATAREDUX (ANR-19-CE46-0008).

6 Competing Interests

The authors have declared that no competing interests exist.

7 Data availability statement

The conditions of our ethics approval do not permit public archiving of anonymised study data. Readers seeking access to the data should contact Dr. Agnès Trebuchon (agnes.trebuchon@univ-amu.fr). Access will be granted to named individuals in accordance with ethical procedures governing the reuse of clinical data, including completion of a formal data sharing agreement.

References

1. R. Abreu, A. Leal, and P. Figueiredo. Identification of epileptic brain states by dynamic functional connectivity analysis of simultaneous EEG-fMRI: a dictionary learning approach. *Scientific Reports*, 9(1):638, 2019.

2. E. A. Allen, E. Damaraju, S. M. Plis, E. B. Erhardt, T. Eichele, and V. D. Calhoun. Tracking Whole-Brain Connectivity Dynamics in the Resting State. *Cerebral Cortex*, 24(3), 11 2012.

3. J. Bancaud. La stéréo-électroencéphalographie dans l'épilepsie: informations neurophysiopathologiques apportées par l'investigation fonctionnelle stéreotaxique: rapport présenté a la société d'électroencéphalographie de langue francaise (marseille, octobre 1962). *(No Title)*, 1965.

4. S. K. Bandt, P. Besson, B. Ridley, F. Pizzo, R. Carron, J. Regis, F. Bartolomei, J. P. Ranjeva, and M. Guye. Connectivity strength, time lag structure and the epilepsy network in resting-state fmri. *NeuroImage: Clinical*, 24:102035, 2019.

5. F. Bartolomei, M. Guye, and F. Wendling. Abnormal binding and disruption in large scale networks involved in human partial seizures. *EPJ Nonlinear Biomedical Physics*, 1(1):4, 2013.

6. F. Bartolomei, S. Lagarde, F. Wendling, A. McGonigal, V. Jirsa, M. Guye, and C. BÃ©nar. Defining epileptogenic networks: Contribution of seeg and signal analysis. *Epilepsia*, 58(7):1131–1147, 2017.

7. D. S. Bassett, M. A. Porter, N. F. Wymbs, S. T. Grafton, J. M. Carlson, and P. J. Mucha. Robust detection of dynamic community structure in networks. *Chaos: An Interdisciplinary Journal of Nonlinear Science*, 23(1):013142, 2013.

8. A. M. Bastos, J. Vezoli, C. A. Bosman, J.-M. Schoffelen, R. Oostenveld, J. R. Dowdall, P. D. Weerd, H. Kennedy, and P. Fries. Visual Areas Exert Feedforward and Feedback Influences through Distinct Frequency Channels. *Neuron*, 85(2):390 401, 01 2015.

9. D. Battaglia, T. Boudou, E. C. Hansen, D. Lombardo, S. Chettouf, A. Daffertshofer, A. R. McIntosh, J. Zimmermann, P. Ritter, and V. Jirsa. Dynamic functional connectivity between order and randomness and its evolution across the human adult lifespan. *NeuroImage*, 222:117156, 2020.

10. J. M. Beggs and D. Plenz. Neuronal avalanches in neocortical circuits. *Journal of Neuroscience*, 23(35):11167 – 11177, 12 2003.

11. A. Bernacchia, H. Seo, D. Lee, and X.-J. Wang. A reservoir of time constants for memory traces in cortical neurons. *Nature Neuroscience*, 14(3):366 – 372, 03 2011.

12. V. D. Blondel, J.-L. Guillaume, R. Lambiotte, and E. Lefebvre. Fast unfolding of communities in large networks. *Journal of Statistical Mechanics: Theory and Experiment*, 2008(10):P10008, oct 2008.

13. W. Clawson, A. F. Vicente, M. Ferraris, C. Bernard, D. Battaglia, and P. P. Quilichini. Computing hubs in the hippocampus and cortex. *Science Advances*, 5(6), 2019.

14. S. Courtens, B. Colombet, A. TrÃ©buchon, A. Brovelli, F. Bartolomei, and C. G. BÃ©nar. Graph measures of node strength for characterizing preictal synchrony in partial epilepsy. *Brain Connectivity*, 6(7):530–539, 2016. PMID: 27140287.

15. J. P. Crutchfield. Between order and chaos. *Nature Physics*, 8(1):17 24, 12 2011.

16. J. Faskowitz, F. Z. Esfahlani, Y. Jo, O. Sporns, and R. F. Betzel. Edge-centric functional network representations of human cerebral cortex reveal overlapping system-level architecture. *Nature neuroscience*, 23(12):1644–1654, 9 2019.

17. A. Fasola, F.-X. Alario, M. Tellier, B. Giusiano, C. A. Tassinari, F. Bartolomei, and A. TrÃ©buchon. A description of verbal and gestural communication during postictal aphasia. *Epilepsy & Behavior*, 102:106646, 2020.

18. S. Fortunato. Community detection in graphs. *Physics Reports*, 486(3):75 – 174, 2010.

19. P. Fries. Rhythms for Cognition: Communication through Coherence. *Neuron*, 88(1):220 235, 10 2015.

20. A.-L. Giraud and D. Poeppel. Cortical oscillations and speech processing: emerging computational principles and operations. *Nature Neuroscience*, 15(4):511–517, 2012.

21. X. He, D. S. Bassett, G. Chaitanya, M. R. Sperling, L. Kozlowski, and J. I. Tracy. Disrupted dynamic network reconfiguration of the language system in temporal lobe epilepsy. *Brain*, 141(5):1375–1389, 2018.

22. V. K. Jirsa, W. C. Stacey, P. P. Quilichini, A. I. Ivanov, and C. Bernard. On the nature of seizure dynamics. *Brain*, 137(Pt 8):2210 2230, 2014-08.

23. C. Kirst, M. Timme, and D. Battaglia. Dynamic information routing in complex networks. *Nature communications*, 7(1):11061, 2016.

24. A. Kumar, S. Rotter, and A. Aertsen. Conditions for propagating synchronous spiking and asynchronous firing rates in a cortical network model. *The Journal of neuroscience : the official journal of the Society for Neuroscience*, 28(20):5268 – 5280, 05 2008.

25. J.-P. Lachaux, A. Lutz, D. Rudrauf, D. Cosmelli, M. Le Van Quyen, J. Martinerie, and F. Varela. Estimating the time-course of coherence between single-trial brain signals: an introduction to wavelet coherence. *Neurophysiologie Clinique/Clinical Neurophysiology*, 32(3):157–174, 2002.

26. S. Lagarde, N. Roehri, I. Lambert, A. Trebuchon, A. McGonigal, R. Carron, D. Scavarda, M. Milh, F. Pizzo, B. Colombet, B. Giusiano, S. Medina Villalon, M. Guye, C.-G. Bénar, and F. Bartolomei. Interictal stereotactic-EEG functional connectivity in refractory focal epilepsies. *Brain*, 141(10):2966–2980, 08 2018.

27. Q.-H. Liu, X. Xiong, Q. Zhang, and N. Perra. Epidemic spreading on time-varying multiplex networks. *Phys. Rev. E*, 98:062303, Dec 2018.

28. D. Lombardo, C. CassÃ©-Perrot, J.-P. Ranjeva, A. Le Troter, M. Guye, J. Wirsich, P. Payoux, D. BartrÃ©s-Faz, R. Bordet, J. C. Richardson, O. Felician, V. Jirsa, O. Blin, M. Didic, and D. Battaglia. Modular slowing of resting-state dynamic functional connectivity as a marker of cognitive dysfunction induced by sleep deprivation. *NeuroImage*, 222:117155, 2020.

29. N. Masuda and P. Holme. Detecting sequences of system states in temporal networks. *Scientific Reports*, 9(1):795, 2019.

30. L. Meyer. The neural oscillations of speech processing and language comprehension: state of the art and emerging mechanisms. *European Journal of Neuroscience*, 48(7):2609–2621, 2018.

31. G. Michalareas, J. Vezoli, S. v. Pelt, J.-M. Schoffelen, H. Kennedy, and P. Fries. Alpha-Beta and Gamma Rhythms Subserve Feedback and Feedforward Influences among Human Visual Cortical Areas. *Neuron*, 89(2):384 397, 01 2016.

32. P. J. Mucha, T. Richardson, K. Macon, M. A. Porter, and J.-P. Onnela. Community structure in time-dependent, multiscale, and multiplex networks. *Science*, 328(5980):876–878, 2010.

33. Y. Nir, L. Fisch, R. Mukamel, H. Gelbard-Sagiv, A. Arieli, I. Fried, and R. Malach. Coupling between neuronal firing rate, gamma LFP, and BOLD fMRI is related to interneuronal correlations. *Current biology : CB*, 17(15):1275 – 1285, 08 2007.

34. A. Palmigiano, T. Geisel, F. Wolf, and D. Battaglia. Flexible information routing by transient synchrony. *Nature Neuroscience*, 20(7):1014 1022, 2017-07.

35. F. Pedregosa, G. Varoquaux, A. Gramfort, V. Michel, B. Thirion, O. Grisel, M. Blondel, P. Prettenhofer, R. Weiss, V. Dubourg, J. Vanderplas, A. Passos, D. Cournapeau, M. Brucher, M. Perrot, and E. Duchesnay. Scikit-learn: Machine learning in Python. *Journal of Machine Learning Research*, 12:2825–2830, 2011.

36. N. Pedreschi, D. Battaglia, and A. Barrat. The temporal rich club phenomenon. *Nature Physics*, 18(8):931–938, 2022.

37. N. Pedreschi, C. Bernard, W. Clawson, P. Quilichini, A. Barrat, and D. Battaglia. Dynamic core-periphery structure of information sharing networks in entorhinal cortex and hippocampus. *Network Neuroscience*, 4(3):946–975, 09 2020.

38. C. J. Price. A review and synthesis of the first 20 years of pet and fmri studies of heard speech, spoken language and reading. *Neuroimage*, 62(2):816–847, 2012.

39. S. Ray, N. E. Crone, E. Niebur, P. J. Franaszczuk, and S. S. Hsiao. Neural Correlates of High-Gamma Oscillations (60-200 Hz) in Macaque Local Field Potentials and Their Potential Implications in Electrocorticography. *Journal of Neuroscience*, 28(45):11526–11536, 2008.

40. M. L. Saggio, D. Crisp, J. M. Scott, P. Karoly, L. Kuhlmann, M. Nakatani, T. Murai, M. Dºmpelmann, A. Schulze-Bonhage, A. Ikeda, M. Cook, S. V. Gliske, J. Lin, C. Bernard, V. Jirsa, and W. C. Stacey. A taxonomy of seizure dynamotypes. *eLife*, 9:e55632, 2020.

41. B. H. Scheid, A. Ashourvan, J. Stiso, K. A. Davis, F. Mikhail, F. Pasqualetti, B. Litt, and D. S. Bassett. Time-evolving controllability of effective connectivity networks during seizure progression. *Proceedings of the National Academy of Sciences*, 118(5):e2006436118, 2021.